

**Postbounce evolution of core-collapse supernovae:
Long-term effects of equation of state**

K. Sumiyoshi

*Numazu College of Technology,
Ooka 3600, Numazu, Shizuoka 410-8501, Japan*

`sumi@numazu-ct.ac.jp`

S. Yamada

*Science and Engineering, Waseda University,
Okubo, 3-4-1, Shinjuku, Tokyo 169-8555, Japan*

&

*Advanced Research Institute for Science and Engineering, Waseda University,
Okubo, 3-4-1, Shinjuku, Tokyo 169-8555, Japan*

H. Suzuki

*Faculty of Science and Technology, Tokyo University of Science,
Yamazaki 2641, Noda, Chiba 278-8510, Japan*

H. Shen

*Department of Physics, Nankai University,
Tianjing 300071, China*

S. Chiba

*Advanced Science Research Center,
Japan Atomic Energy Research Institute,
Tokai, Ibaraki 319-1195, Japan*

and

H. Toki

*Research Center for Nuclear Physics (RCNP), Osaka University,
Mihogaoka 10-1, Ibaraki, Osaka 567-0047, Japan*

ABSTRACT

We study the evolution of supernova core from the beginning of gravitational collapse of a $15M_{\odot}$ star up to 1 second after core bounce. We present results of spherically symmetric simulations of core-collapse supernovae by solving general relativistic ν -radiation-hydrodynamics in the implicit time-differencing. We aim to explore the evolution of shock wave in a long term and investigate the formation of protoneutron star together with supernova neutrino signatures. These studies are done to examine the influence of equation of state (EOS) on the postbounce evolution of shock wave in the late phase and the resulting thermal evolution of protoneutron star. We make a comparison of two sets of EOS, that is, by Lattimer and Swesty (LS-EOS) and by Shen et al.(SH-EOS). We found that, for both EOSs, the core does not explode and the shock wave stalls similarly in the first 100 milliseconds after bounce. The revival of shock wave does not occur even after a long period in either cases. However, the recession of shock wave appears different beyond 200 milliseconds after bounce, having different thermal evolution of central core. A more compact protoneutron star is found for LS-EOS than SH-EOS with a difference in the central density by a factor of ~ 2 and a difference of ~ 10 MeV in the peak temperature. Resulting spectra of supernova neutrinos are different to the extent that may be detectable by terrestrial neutrino detectors.

Subject headings: supernovae: general — stars: neutron — neutrinos — hydrodynamics — equation of state

1. Introduction

Understanding the explosion mechanism of core-collapse supernovae is a grand challenge that requires endeavor to conduct numerical simulations of ν -radiation-hydrodynamics with best knowledge of particle and nuclear physics. Three dimensional simulations of ν -radiation-hydrodynamics, which are currently formidable, and better determinations of the nuclear equation of state of dense matter and the neutrino-related reaction rates are mandatory. One has to advance step by step by developing numerical methods and examining microphysics and its influence in various stages of supernovae.

Even with the extensive studies in recent years with currently available computing resources, the numerical results have not made clear the explosion mechanism. On one hand, recent multi-dimensional supernova simulations with approximate neutrino-transport

schemes have revealed the importance of asymmetry such as rotation, convection, magnetic fields and/or hydrodynamical instability (Blondin et al. 2003; Buras et al. 2003; Kotake et al. 2003; Fryer & Warren 2004; Kotake et al. 2004; Walder et al. 2004). On the other hand, spherically symmetric supernova simulations of late have removed the uncertainty of neutrino-transport and clarified the role of neutrinos in core-collapse and shock propagation (Rampp & Janka 2000; Liebendörfer et al. 2001; Mezzacappa et al. 2001; Rampp & Janka 2002; Thompson et al. 2003). In this study, we focus on spherically symmetric simulations which are advantageous to examine the role of microphysics without ambiguity of neutrino-transport.

Almost all authors have reported that neither prompt explosion nor delayed explosion occurs under the spherical symmetry. This conclusion is commonly reached by simulations with Newtonian (Rampp 2000; Rampp & Janka 2000; Mezzacappa et al. 2001; Thompson et al. 2003), approximately relativistic (Rampp & Janka 2002) and fully general relativistic (Liebendörfer et al. 2001) gravity, together with standard microphysics, i.e. the equation of state (EOS) by Lattimer & Swesty (1991) and the weak reaction rates by Bruenn (1985). The influence of nuclear physics inputs has been further assessed by employing the extended neutrino reactions (Thompson et al. 2003, see also section 3.2) and more up-to-date electron capture rates on nuclei (Hix et al. 2003). The dependence on the progenitor models (Liebendörfer et al. 2002; Thompson et al. 2003; Liebendörfer et al. 2004; Janka et al. 2004) and the sets of physical EOS (Janka et al. 2004) has been studied very recently. These simulations so far have shown that the collapse of iron cores leads to the stalled shock after bounce without successful explosion.

In the current study, we explore the influence of EOS in the time period that has not been studied very well in the previous studies. Most of recent numerical simulations have been performed until about 300 milliseconds after bounce. This is due to the severe limitation on time steps by the Courant condition for explicit time-differencing schemes. A typical time step in the explicit method is about 10^{-6} seconds after the formation of dense compact objects. However, in the implicit method as we employ in this study, the time step is not restricted by the Courant condition. This is advantageous for a long-term evolution. In the studies by Liebendörfer et al. (2002, 2004), who also adopted the implicit method, the postbounce evolution has been followed up to about 1 second for a small number of models with Lattimer and Swesty EOS. Historically, the idea of the delayed explosion was proposed by Wilson’s simulations that followed more than several hundred milliseconds after bounce. In some cases, the revival of shock wave occurred even beyond 0.5 seconds (for example, Bethe and Wilson 1985). It is still interesting to explore this late phase in the light of possible influence of microphysics.

The progress of the supernova EOS put an additional motivation to the study of this late postbounce phase. Only recently the sets of physical EOS, which cover a wide range of density, composition and temperature in a usable and complete form, have become available for simulations. A table of EOS was made for the first time by Hillebrandt & Wolff (1985) within the Skyrme Hartree-Fock approach and applied to some simulations (Hillebrandt et al. 1984; Suzuki 1990, 1993, 1994; Sumiyoshi et al. 1995c; Janka et al. 2004). Another set of EOS has been provided as a numerical routine by Lattimer & Swesty (1991) utilizing the compressible liquid-drop model. This EOS has been used these years as a standard.

Recently, a new complete set of EOS for supernova simulations has become available (Shen et al. 1998a,b). The relativistic mean field (RMF) theory with a local density approximation was applied to the derivation of the table of supernova EOS. This EOS is different in two important aspects from previous EOSs. One thing is that the Shen’s EOS is based on the relativistic nuclear many-body framework whereas the previous ones are based on the non-relativistic frameworks. The relativistic treatment is known to affect the behavior of EOS at high densities (i.e. stiffness) (Brockmann & Machleidt 1990) and the size of nuclear symmetry energy (Sumiyoshi et al. 1995b). The other thing is that the Shen’s EOS is based on the experimental data of unstable nuclei, which have become available recently. The data of neutron-rich nuclei, which are close to the astrophysical environment, were used to constrain the nuclear interaction. The resulting properties of isovector interaction are generally different from the non-relativistic counterpart and the size of symmetry energy is different. The significant differences in stiffness and compositions during collapse and bounce have been shown between Shen’s EOS and Lattimer-Swesty EOS by hydrodynamical calculations (Sumiyoshi et al. 2004). Therefore, it would be exciting to explore the supernova dynamics with the new set of EOS. Such an attempt has been made recently by Janka et al. (2004) and no explosion has been reported up to 300 milliseconds after bounce.

Our aim of the current study is, therefore, the comparison of the postbounce evolutions beyond 300 milliseconds for the first time. We perform the core-collapse simulations adopting the two sets of EOS, that is, Shen’s EOS (SH-EOS) and Lattimer-Swesty EOS (LS-EOS). We follow the evolutions of supernova core for a long period. We explore the fate of the stalled shock up to 1 second after bounce. In this time period, one can also see the birth of protoneutron star as a continuous evolution from the collapsing phase together with the long-term evolution of neutrino emissions. Although the supernova core does not display successful explosion, as we will see, the current simulations may provide some aspects of central core leading to the formation of protoneutron star or black hole. This information is also helpful to envisage the properties of supernova neutrinos in the first second since the simulations of protoneutron star cooling done so far usually starts from several hundred milliseconds after bounce for some given profiles. As a whole, we aim to clarify how the EOS

influences the dynamics of shock wave, evolution of central core and supernova neutrinos.

2. Numerical Methods

A new numerical code of general relativistic, ν -radiation-hydrodynamics under the spherical symmetry has been developed (Yamada 1997; Yamada et al. 1999) for supernova simulations. The code solves a set of equations of hydrodynamics and neutrino-transfer simultaneously in the implicit way, which enables us to have substantially longer time steps than explicit methods. This is advantageous for the study of long-term behaviors after core bounce. The implicit method has been also adopted by Liebendörfer et al. (2004) in their general relativistic ν -radiation-hydrodynamics code. They have taken, however, an operator splitting method so that hydrodynamics and neutrino-transfer could be treated separately.

2.1. Hydrodynamics

The equations of lagrangian hydrodynamics in general relativity are solved by a implicit, finite differencing. The numerical method is based on the approximate linearized Riemann solver (Roe-type scheme) that captures shock waves without introducing artificial viscosities. Assuming the spherical symmetry, the metric of Misner & Sharp (1964) is adopted to formulate hydrodynamics and neutrino-transport equations. A set of equations for the conservation of baryon number, lepton number and energy-momentum are solved together with the metric equations and the entropy equation. Details of the numerical method of hydrodynamics can be found in (Yamada 1997), where standard numerical tests of the hydrodynamics code have been also reported.

2.2. Neutrino-transport

The Boltzmann equation for neutrinos in general relativity is solved by a finite difference scheme (S_N method) implicitly together with above-mentioned lagrangian hydrodynamics. The neutrino distribution function, $f_\nu(t, m, \mu, \varepsilon_\nu)$, as a function of time t , lagrangian mass coordinate m , neutrino propagation angle μ and neutrino energy ε_ν , is evolved. Finite differencing of the Boltzmann equation is mostly based on the scheme by Mezzacappa & Bruenn (1993a). However, the update of time step is done simultaneously with hydrodynamics. The reactions of neutrinos are explicitly calculated in the collision terms of the Boltzmann equation with incident/outgoing neutrino angles and energies taken into account. Detailed

comparisons with the Monte Carlo method have been made to validate the Boltzmann solver and to examine the angular resolution (Yamada et al. 1999).

2.3. ν -radiation-hydrodynamics

The whole set of finite-differenced equations described above are solved by the Newton-Raphson iterative method. The Jacobian matrix forms a block-tridiagonal matrix, in which dense block matrices arise from the collision terms of the transport equation. Since the inversion of this large matrix is most costly in the computing time, we utilize a parallel algorithm of block cyclic reduction for the matrix solver (Sumiyoshi & Ebisuzaki 1998). In the current simulations, we adopt non-uniform 255 spatial zones for lagrangian mass coordinate. We discretize the neutrino distribution function with 6 angle zones and 14 energy zones for ν_e , $\bar{\nu}_e$, $\nu_{\mu/\tau}$ and $\bar{\nu}_{\mu/\tau}$, respectively.

2.4. Rezoning

The description of long-term evolution of accretion in a lagrangian coordinate is a numerically tough problem. In order to keep enough resolution during the accretion phase, rezoning of accreting materials is done long before they accrete onto the surface of protoneutron star and become opaque to neutrinos. At the same time, dezoning of the hydrostatic inner part of protoneutron star is done to avoid the increase of grid points.

When we have tried simulations without rezoning, neutrino luminosities oscillate largely in time due to intermittent accretion of coarse grid points and it sometimes leads to erroneous dynamics (even explosions). Therefore, we have checked that the resolution of grid points is enough by refining the initial grid points and rezoning during the simulations. Even then, there are still slight oscillations in luminosities and average energies of neutrinos in the last stage of calculations. There are also transient kinks sometimes when the grid size in mass coordinate changes during accretion as we will see in section 4.5. These slight modulations of neutrino quantities, however, do not affect the overall evolution of protoneutron stars with accretion once we have enough resolution.

3. Model Descriptions

As an initial model, we adopt the profile of iron core of a $15M_{\odot}$ progenitor from Woosley & Weaver (1995). This progenitor has been widely used in supernova simulations. The

computational grid points in mass coordinate are non-uniformly placed to cover the central core, shock propagation region and accreting material with enough resolution.

3.1. Equation of state

The new complete set of EOS for supernova simulations (SH-EOS) (Shen et al. 1998a,b) is derived by the relativistic mean field (RMF) theory with a local density approximation. The RMF theory has been a successful framework to reproduce the saturation properties, masses and radii of nuclei, and proton-nucleus scattering data (Serot & Walecka 1986). We stress that the RMF theory (Sugahara & Toki 1994) is based on the relativistic Brückner-Hartree-Fock (RBHF) theory (Brockmann & Machleidt 1990), which is a microscopic and relativistic many-body theory. The RBHF theory has been shown to be successful to reproduce the saturation of nuclear matter starting from the nucleon-nucleon interactions determined by scattering experiments. This is in good contrast with non-relativistic many-body frameworks which can account for the saturation only with the introduction of extra three-body interactions.

The effective interactions in the RMF theory have been determined by least squares fittings to reproduce the experimental data of masses and radii of stable and unstable nuclei (Sugahara & Toki 1994). The determined parameters of interaction, TM1, have been applied to many studies of nuclear structures and experimental analyses (Sugahara et al. 1996; Hirata et al. 1997). One of stringent tests on the isovector interaction is passed in excellent agreement of the theoretical prediction with the experimental data on neutron and proton distributions in isotopes including neutron-rich ones with neutron-skins (Suzuki et al. 1995; Ozawa et al. 2001). The RMF theory with the parameter set TM1 provides uniform nuclear matter with the incompressibility of 281 MeV and the symmetry energy of 36.9 MeV. The maximum mass of neutron star is $2.2 M_{\odot}$ for the cold neutron star matter in the RMF with TM1 (Sumiyoshi et al. 1995a). The table of EOS covers a wide range of density, electron fraction and temperature for supernova simulations, and has been applied to numerical simulations of r-process in neutrino-driven winds (Sumiyoshi et al. 2000), prompt supernova explosions (Sumiyoshi et al. 2001), and other simulations (Sumiyoshi et al. 1995c; Rosswog & Davies 2003; Sumiyoshi et al. 2004; Janka et al. 2004).

For comparison, we also adopt the EOS by Lattimer & Swesty (1991). The LS-EOS is based on the compressible liquid drop model for nuclei together with dripped nucleons. The bulk energy of nuclear matter is expressed in terms of density, proton fraction and temperature. The values of nuclear parameters are chosen according to nuclear mass formulae and other theoretical studies with the Skyrme interaction. Among various parameters, the

symmetry energy is set to be 29.3 MeV, which is smaller than the value in the relativistic EOS. As for the incompressibility, we use 180 MeV, which has been used frequently for recent supernova simulations. In this case, the maximum mass of neutron star is estimated to be $1.8 M_{\odot}$. This choice enables us to make comparisons with previous works, though 180 MeV is smaller than the standard value as will be discussed below. The sensitivity to the incompressibility of LS-EOS has been studied by Thompson et al. (2003) using the choices of 180, 220 and 375 MeV. The numerical results of core-collapse and bounce with different incompressibilities turn out to be similar up to 200 milliseconds after bounce. The differences in luminosities and average energies of emergent neutrinos are within 10 % and do not affect significantly the post-bounce dynamics on the time scale of 100 ms. The influence of different incompressibilities in LS-EOS on the time scale of 1 sec remains to be seen as an extension of the current study. For densities below 10^7 g/cm³, the subroutine of Lattimer-Swesty EOS runs into numerical troubles, therefore, we adopt Shen’s EOS in this density regime instead. This is mainly for numerical convenience. In principle, it is preferable to adopt the EOS, which contains electrons and positrons at arbitrary degeneracy and relativity, photons, nucleons and an ensemble of nuclei as non-relativistic ideal gases (see for example, Timmes & Arnett (1999); Thompson et al. (2003)). One also has to take into account non-NSE abundances determined from the preceding quasi-static evolutions. Note that we are chiefly concerned with the effect of EOS at high densities, and this pragmatic treatment does not have any significant influence on the shock dynamics.

We comment here on the nuclear parameters of EOS and its consequences for the astrophysical applications considered here. The value of incompressibility of nuclear matter has been considered to be within 200–300 MeV from experimental data and theoretical analyses. The value recently obtained within the non-relativistic approaches (Colo & Van Giai 2004) is 220–240 MeV. The corresponding value extracted within the relativistic approaches is known to be higher than non-relativistic counterpart and is 250–270 MeV (Vretenar et al. 2003; Colo & Van Giai 2004). It is also known that the determination of incompressibility is closely related with the size of the symmetry energy and its density dependence. The incompressibility of EOS in the RMF with TM1 is slightly higher than those standard values and the SH-EOS is relatively stiff. The neutron stars with SH-EOS are, therefore, less compact with lower central densities and have higher maximum masses than those obtained by LS-EOS with the incompressibility of 180 MeV. The adiabatic index of SH-EOS at the bounce of supernova core is larger than that of LS-EOS (Sumiyoshi et al. 2004).

The value of symmetry energy at the nuclear matter density is known to be around 30 MeV by nuclear mass formulae (Möller et al. 1995). The recent derivation of the symmetry energy in a relativistic approach gives higher values of 32–36 MeV together with the above mentioned higher incompressibility (Dieperink et al. 2003; Vretenar et al. 2003). The sym-

metry energy in the RMF with TM1 is still a bit larger compared with the standard values. We note that the symmetry energy in the RMF is determined by the fitting of masses and radii of various nuclei including neutron-rich ones. The large symmetry energy in SH-EOS leads to large proton fractions in cold neutron stars, which may lead to a possible rapid cooling by the direct URCA process, as well as the stiffness of neutron matter (Sumiyoshi et al. 1995a). The difference between neutron and proton chemical potentials is large and leads to different compositions of free protons and nuclei (Sumiyoshi et al. 2004). The consequences of these differences in incompressibility and symmetry energy will be discussed in the comparison of numerical simulations in section 4.

3.2. Weak reaction rates

The weak interaction rates regarding neutrinos are evaluated by following the standard formulation by Bruenn (1985). For the collision term in the Boltzmann equation, the scattering kernels are explicitly calculated in terms of angles and energies of incoming and outgoing neutrinos (Mezzacappa & Bruenn 1993b). In addition to the Bruenn’s standard neutrino processes, the plasmon process (Braaten and Segel 1993) and the nucleon-nucleon bremsstrahlung process (Friman & Maxwell 1979; Maxwell 1987) are included in the collision term. The latter reaction has been shown to be an important process to determine the supernova neutrinos from the protoneutron star cooling (Suzuki 1993; Burrows et al. 2000) as a source of $\nu_{\mu/\tau}$. The conventional *standard* weak reaction rates are used for the current simulations to single out the effect of EOS and to compare with previous simulations. Recent progress of neutrino opacities in nuclear matter (Burrows et al. 2005) and electron capture rates on nuclei (Langanke & Martinez-Pinedo 2003) will be examined along with the updates of EOS in future studies.

4. Comparison of results

We present the results of two numerical simulations performed with Shen’s EOS and Lattimer-Swesty EOS. They are denoted by SH and LS, respectively.

4.1. Shock propagation

Fig. 1 shows the radial trajectories of mass elements as a function of time after bounce in model SH. The trajectories are plotted for each $0.02M_{\odot}$ in mass coordinate up to $1.0M_{\odot}$

and for each $0.01M_{\odot}$ for the rest of outer part. Thick lines denote the trajectories for $0.5M_{\odot}$, $1.0M_{\odot}$ and $1.5M_{\odot}$. One can see the shock wave is launched up to 150 kilometers and stalled there within 100 milliseconds. The shock wave recedes down to below 100 kilometers afterwards and the revival of shock wave or any sign of it is not found even after 300 milliseconds.

Instead, the stationary accretion shock is formed at several tens of kilometers. As the central core gradually contracts, a protoneutron star is born at center. The material, which was originally located in the outer core, accretes onto the surface of the protoneutron star. The accretion rate is about $0.2M_{\odot}/s$ on average and decreases from $0.25M_{\odot}/s$ to $0.15M_{\odot}/s$ gradually. This behavior is similar in model LS. At 1 sec after bounce, the baryon mass of protoneutron star is $1.60M_{\odot}$ for both cases.

The trajectories of shock wave in models SH and LS are compared in Fig. 2. The propagations of shock wave in two models are similar in the first 200 milliseconds (left panel). We note that slight fluctuations in the curves are due to numerical artifact in the procedure to determine the shock position. Note that we have rather low resolutions in the central part in order to have higher resolutions in the accreting material. Except for the discrepancy due to the different numerical methods (e.g. approximate general relativity, eulerian etc.), zoning and resolutions, the current simulations up to 200 milliseconds are consistent with the results (middle panel of Figure 3) by Janka et al. (2004) having similar maximum radii and timing of recession. The difference shows up from 200 milliseconds after bounce and becomes more apparent in the later phase (right panel). After 600 milliseconds, the shock position in model LS is less than 20 kilometers and it is clearly different from that in model SH. This difference originates from the faster contraction of the protoneutron star in model LS. We discuss the evolution of protoneutron star later in section 4.4.

4.2. Collapse phase

The initial propagation of shock wave is largely controlled by the properties of the inner core during the gravitational collapse. We have found noticeable differences in the behavior of core-collapse in two models. However, they did not change the initial shock energy drastically, which then leads to the similarity of the early phase of shock propagation we have just seen above.

First of all, it is remarkable that the compositions of dense matter during the collapse are different. In Fig. 3, the mass fraction is shown as a function of mass coordinate when the central density reaches 10^{11} g/cm³. The mass fraction of free proton in model SH is

smaller than that in model LS by a factor of ~ 5 . This is caused by the larger symmetry energy in SH-EOS, where the proton chemical potential is lower than the neutron chemical potential as discussed in Sumiyoshi et al. (2004). The smaller free proton fraction reduces the electron captures on free protons. Note that the electron capture on nuclei is suppressed in the current simulations due to the blocking above $N=40$ in Bruenn’s prescription. This is in accordance with the numerical results by Bruenn (1989); Swesty et al. (1994) who studied the influence of the free proton fraction and the symmetry energy. However, there is also a negative feedback in the deleptonization during collapse (Liebendörfer et al. 2002). Smaller electron capture rates keep electron fraction high, which then leads to an increase of free proton fraction and consequently to electron captures after all. The resultant electron fraction turns out to be not significantly different as we will see later.

It is also noticeable that the mass fraction of alpha particles differs substantially and the abundance of nuclei is slightly reduced in model SH. This difference of alpha abundances in two models persists during the collapse and even in the post-bounce phase. The nuclear species appearing in the central core during collapse are shown in the nuclear chart (Fig. 4). The nuclei in model SH are always less neutron-rich than those in model LS by more than several neutrons. This is also due to the effect of the symmetry energy, which gives nuclei closer to the stability line in model SH. The mass number reaches up to ~ 80 and ~ 100 at the central density of 10^{11} g/cm³ (solid circle) and 10^{12} g/cm³ (open circle), respectively. In the current simulations, the electron capture on nuclei is suppressed beyond $N=40$ due to the simple prescription employed here and the difference of species do not give any difference. However, results may turn out different when more realistic electron capture rates are adopted (Hix et al. 2003). It would be interesting to see whether the difference found in two EOSs leads to differences in central cores using recent electron capture rates on nuclei (Langanke & Martinez-Pinedo 2003). Further studies are necessary to discuss the abundances of nuclei and the influence of more updated electron capture rates for mixture of nuclear species beyond the approximation of single-species in the current EOSs.

The profiles of lepton fractions at bounce are shown in Fig. 5. The central electron fraction in model SH is $Y_e=0.31$, which is slightly higher than $Y_e=0.29$ in model LS. The central lepton fractions including neutrinos for models SH and LS are rather close to each other, having $Y_L=0.36$ and 0.35 , respectively. The difference of lepton fraction results in a different size of the inner core. The larger lepton fraction in model SH leads to a larger inner core $0.61M_\odot$, whereas it is $0.55M_\odot$ in model LS. Here, the inner core is defined by the region inside the position of velocity discontinuity, which is the beginning of shock wave. Fig. 6 shows the velocity profile at bounce. We define the bounce ($t_{pb}=0$ ms) as the time when the central density reaches the maximum, which is similar to other definitions such as using the peak entropy height. The central density reaches 3.4×10^{14} g/cm³ and 4.4×10^{14}

g/cm^3 in models SH and LS, respectively. The difference of stiffness in two EOSs leads to a lower peak central density in model SH than that in model LS. Because of this difference, the radial size of inner core at bounce is ~ 1 km larger for model SH than that for model LS.

The initial shock energy, which is roughly estimated by the gravitational binding energy of inner core at bounce, turns out to be not drastically different because of the increases both in mass and radial size of the inner core in model SH. Clearer difference appears at later stages where the protoneutron star is formed having a central density much higher than the nuclear matter density. This is one of reasons why we are interested in the late phase of supernova core, where the difference of EOS appears more clearly and its influence on the supernova dynamics could be seen.

We remark here that the numerical results with LS-EOS at bounce are in good agreement with previous simulations such as the reference models by Liebendörfer et al. (2005). For example, the profiles of model LS shown in Figs. 5 and 6 accord with the profiles of their model G15. The behavior after bounce is also qualitatively consistent with the reference models up to 250 milliseconds (see also section 4.4).

4.3. Postbounce phase

The postbounce phase is interesting in many aspects, especially in clarifying the role of EOS in the neutrino heating mechanism and the protoneutron star formation. As we have seen in section 4.1, the stall of shock wave occurs in a similar manner in two models and the difference appears in later stage. We discuss here the similarities and the differences in terms of the effect of EOS.

The evolution of shock wave after it stalls around 100 kilometers is controlled mainly by the neutrino heating behind the shock wave. The neutrinos emitted from the neutrinosphere in the nascent protoneutron star contribute to the heating of material just behind the shock wave through absorption on nucleons. Whether the shock wave revives or not depends on the total amount of heating, hence more specifically, on the neutrino spectrum, luminosity, amount of targets (nucleons), mass of heating region and duration time.

The heating rates of material in supernova core in two models at $t_{pb}=150$ ms are shown in Fig. 7 as a function of radius. The heating rate in model SH is smaller than that in model LS around 100 kilometers. The cooling rate (negative value in the heating rate) in model SH is also smaller than that in model LS. The smaller heating (cooling) rate in model SH is caused by lower neutrino luminosities and smaller free-proton fractions. Figs. 8 and 9 show the radial profiles of neutrino luminosities and mass fractions of dense matter around

the heating region. The luminosities in model SH are lower than those in model LS for all neutrino flavors. The mass fraction of free protons, which are the primary target of neutrino heating, is slightly smaller in model SH around the heating region. These two combinations lower the heating rate in model SH. It is also interesting that other compositions (alpha and nuclei) appear different in this region.

The lower luminosities in model SH are related with the lower cooling rate. The temperature of protoneutron star in model SH is generally lower than that in model LS as shown in Fig. 10. The peak temperature, which is produced by the shock heating and the contraction of core, in model SH is lower than that in model LS. This difference exists also in the surface region of the protoneutron star, where neutrinos are emitted via cooling processes. The temperature at the neutrinosphere in model SH is lower and, as a result, the cooling rate is smaller. The difference of temperature becomes more evident as the protoneutron star evolves as we will see in the next section.

4.4. Protoneutron star

The thermal evolution of protoneutron star formed after bounce is shown in Fig. 11 for two models. Snapshots of temperature profile at $t_{pb}=20, 50, 100, 200, 300, 400, 500, 600, 700, 800, 900$ ms and 1 s are shown. The temperature increase is slower in model SH than in model LS. The peak temperature at $t_{pb}=1$ s is 39 and 53 MeV in models SH and LS, respectively. The temperature difference arises mainly from the stiffness of EOS. The protoneutron star contracts more in model LS and has a higher central density than in model SH. At $t_{pb}=1$ s, the central density in model SH is 4.1×10^{14} g/cm³ whereas that in model LS is 7.0×10^{14} g/cm³, which means the rapid contraction in model LS. Since the profile of entropy per baryon is similar to each other, lower density results in lower temperature. The rapid contraction also gives rise to the rapid recession of shock wave down to 20 kilometers in model LS.

We note here on the effective mass. In SH-EOS, the effective mass of nucleons is obtained from the attraction by scalar mesons in the nuclear many-body framework. The effective mass at center is reduced to be 440 MeV at $t_{pb}=1$ s. The nucleon mass is fixed to be the free nucleon mass in LS-EOS, on the other hand.

The temperature difference within 1 second as we have found may affect the following evolution of protoneutron star up to several tens of seconds, during which the main part of supernova neutrinos is emitted. Although our models do not give a successful explosion, the obtained profiles will still give a good approximation to the initial setup for the subsequent

protoneutron star cooling. Since we have followed the continuous evolution of the central core from the onset of gravitational collapse, the calculated protoneutron star contains the history of matter and neutrinos during the prior stages. This is much better than the situation so far for calculations of protoneutron star cooling, where the profiles from other supernova simulations were adopted for the initial model. It would be interesting to study the cooling of protoneutron star for the two models obtained here. Even if such evolutions of protoneutron star are not associated with a successful supernova explosion, it will be still interesting for the collapsar scenario of GRB and/or black hole formation. Exploratory studies on various scenarios for the fate of compact objects with continuous accretion of matter are fascinating and currently under way, but it is beyond the scope of the present study.

In Fig. 12, we display the profiles of entropy and lepton fraction in model LS at $t_{pb}=100, 250, 500$ ms and 1 s. The distributions of entropy as well as other quantities (not shown here) at $t_{pb}=100$ and 250 ms are consistent with the reference model G15 (Liebendörfer et al. 2005). We have found that the negative gradients in the profiles of entropy and lepton fraction commonly appear in late phase for both models. As for entropy per baryon, the negative gradient appears after $t_{pb}=100$ ms in the region between $\sim 0.7M_{\odot}$ and the shock. The negative gradient of lepton fraction appears first in the outer core behind the shock and then prevails toward the center till $t_{pb}=1$ s. Since these regions are unstable against the convection according to the Ledoux criterion, the whole region of proto-neutron star may be convective after core bounce. It has been pointed out that the sign of derivative of thermodynamical quantities ($\partial\rho/\partial Y_L|_{P,S}$) changes in the neutron-rich environment at high densities beyond 10^{14} g/cm³ (Sumiyoshi et al. 2004), and the central core may be stabilized in model SH. Whether the convection occurs efficiently enough to help the neutrino-driven mechanism for explosion remains to be studied in multi-dimensional ν -radiation-hydrodynamics simulations with SH-EOS.

4.5. Supernova neutrinos

The different temperature distribution could affect the neutrino luminosities and spectra. We discuss here the properties of neutrinos emitted during the evolution of supernova core up to 1 second. As we have already discussed in section 4.3, the luminosity of neutrinos in model SH is lower than that in model LS after bounce. This difference actually appears after $t_{pb}=100$ ms as shown in Fig. 13. The initial rise and peak of luminosities in two models are quite similar to each other. The peak heights of neutronization burst of electron-type neutrino are also similar. The difference, however, gradually becomes larger and apparent

after $t_{pb}=200$ ms. We remark here that the kinks around $t_{pb}=500$ ms are numerical artifact due to the rezoning of mass coordinate as discussed in section 2.4. Except for this kink, the luminosities increase in time. For last 150 milliseconds, luminosities show oscillations numerically, therefore, we have plotted smoothed curves by taking average values. It is to be noted that we are interested in the relative differences of supernova neutrinos between two models.

The difference in average energies of neutrinos appears in a similar manner to that in luminosities as seen in Fig. 14. The average energy presented here is the *rms* average energy, $E_\nu = \sqrt{\langle \varepsilon_\nu^2 \rangle}$, at the outermost grid point (~ 7000 km). The average energies up to $t_{pb}=100$ ms are almost identical in two models and become different from each other afterwards. The average energies in model SH turn out to be lower than those in model LS. Kinks around $t_{pb}=500$ ms appear due to the same reason mentioned above and the curves are smoothed around kinks and $t_{pb} \sim 1$ s to avoid artificial transient behaviors due to the rezoning. At $t_{pb}=1$ s, the gap amounts to be more than a few MeV and has tendency to increase in time. The lower luminosity and average energy in model SH is due to the slow contraction of protoneutron star and, as a result, the slow rise of temperature as seen in Fig. 11. Again, it would be interesting to see the subsequent cooling phase of protoneutron star up to ~ 20 seconds to obtain the main part of supernova neutrinos.

5. Summary

We have performed the numerical simulations of core-collapse supernovae by solving general relativistic ν -radiation-hydrodynamics in spherical symmetry. We have adopted the relativistic EOS table which is based on the recent advancement of nuclear many-body theory as well as the recent experimental data of unstable nuclei, in addition to the conventional Lattimer-Swesty EOS. We have done the long-term simulations from the onset of gravitational collapse to the late phase far beyond 300 milliseconds after bounce, which have not been well studied in previous studies due to the numerical restrictions. This is meant to explore the chance of shock revival and the influence of the new EOS in this stage, and is first such an attempt.

We have found that a successful explosion of supernova core does not occur in neither a prompt nor a delayed way, even though we have followed the postbounce evolution up to 1 second with the new EOS table. The numerical simulation using the Lattimer-Swesty EOS shows no explosion either, which is in accord with other recent studies and in contrast to the finding by Wilson. Note that Wilson incorporated convective effects into their spherical simulations to obtain successful explosions. The shock wave stalls around 100 milliseconds

after bounce and recedes down to several tens of kilometers to form a stationary accretion shock.

Regardless of the outcome with no explosion we have revealed the differences caused by two EOSs in many aspects, which might give some hints for the successful explosion. We have seen the difference in composition of free-protons and nuclei at the collapse phase of supernova core in interesting manners. The difference in symmetry energy of two EOSs has caused this effect, which can change the electron capture rates and the resulting size of bounce cores. Although the early shock propagations turn out to be similar in the current simulations due to the counter effect by the stiffness of EOS and the neutrino heating, the implementation of up-to-date electron capture rates on nuclei is remaining to be done to obtain more quantitatively reliable difference of composition during the collapse phase, which may then affect the initial shock energy.

During the postbounce evolution around 100 milliseconds after bounce we have seen that the heating rates in two models are different due to the different luminosities and compositions predicted by two EOSs. Unfortunately, the merit of larger inner core found in the model with SH-EOS is mostly canceled by the smaller heating rate, and the behaviors of shock wave in the early postbounce phase turn out to be similar in two simulations. In general, though, different heating rates by spectral change of neutrinos and compositional differences due to EOSs might contribute to the revival of shock wave in the neutrino-driven mechanism.

One of the most important facts we have revealed in the comparison is that larger difference actually appears from 200 milliseconds after bounce when the central core contracts to become a protoneutron star. The temperature and density profiles display larger differences as the protoneutron star shrinks further. It is in this late phase that we are interested to see possible influences of EOS for shock dynamics, since the central density becomes high enough and the difference of EOS becomes more apparent. In the current study, we have not found any shock revival in either model. We have found, however, distinctly different thermal evolution of protoneutron stars in two models, and the resulting neutrino spectra are clearly different at this stage. This difference might have some influence on the accretion of matter. The following evolution of protoneutron star cooling or formation of a black hole or any other exotic objects will certainly be affected.

After all, the current numerical simulations of core-collapse supernovae in spherical symmetry have not given successful explosions, even with a new EOS or after long-term evolution. One might argue that this situation indicates the necessity of breaking spherical symmetry, which is also suggested by some observations and has been supported by multi-dimensional simulations. However, before one goes to the conclusion that the asymmetry is

essential in the explosion mechanism, one also has to make efforts to find missing ingredients in microphysics (such as hyperons in EOS, for example) in spherically symmetric simulations. Moreover, the spherical simulations serve as a reliable basis for multi-dimensional computations of ν -radiation-hydrodynamics. Convection may be somehow taken into account effectively in spherical codes as in the stellar evolution codes. These extensions of simulations and microphysics are now in progress. The extension of the relativistic EOS table by including strangeness particles at high densities has been recently made (Ishizuka 2005) and corresponding neutrino reactions in hyperonic matter are currently being implemented in ν -radiation-hydrodynamics.

K. S. expresses thanks to K. Oyamatsu, A. Onishi, K. Kotake, T. Kajino, Tony Mezzacappa and Thomas Janka for stimulating discussions and useful suggestions. K. S. thanks partial supports from MPA in Garching and INT in Seattle where a part of this work has been done. The numerical simulations have been performed on the supercomputers at RIKEN, KEK (KEK Supercomputer Project No. 108), JAERI (VPP5000) and NAO (VPP5000 System Projects yks86c, rks07b, rks52a). This work is supported by the Grant-in Aid for Scientific Research (14039210, 14079202, 14740166, 15540243, 15740160) of the Ministry of Education, Science, Sports and Culture of Japan. This work is partially supported by the Grant-in-Aid for the 21st century COE program "Holistic Research and Education Center for Physics of Self-organizing Systems".

REFERENCES

- Bethe, H. A., & Wilson, J. R. 1985, *ApJ*, 296, 14
- Blondin, J. M., Mezzacappa, A., & DeMarino, C. 2003, *ApJ*, 584, 971
- Braaten, E., & Segel, D. 1993, *Phys. Rev. D*, 48, 1478
- Brockmann, R., & Machleidt, R. 1990, *Phys. Rev. C*, 42, 1965
- Bruenn, S. W. 1985, *ApJS*, 58, 771
- Bruenn, S. W. 1989, *ApJ*, 340, 955
- Buras, R., Rampp, M., Janka, H.-Th., & Kifonidis, K. 2003, *Phys. Rev. Lett.*, 90, 241101
- Burrows, A., Young, T., Pinto, P., Eastman, R., & Thompson, T. A. 2000, *ApJ*, 539, 865
- Burrows, A., Reddy, S. & Thompson, T. A. 2005, *Nucl. Phys. A*, in press

- Colo, G., & Van Giai, N. 2004, *Nucl. Phys. A*, 731, 15
- Dieperink, A. E. L., Dewulf, Y., Van Neck, D., Waroquier, M., & Rodin, V. 2003, *Phys. Rev. C*, 68, 064307
- Friman, B. L., & Maxwell, O. V. 1979, *ApJ*, 232, 541
- Fryer, C. L., & Warren, M. S. 2004, *ApJ*, 601, 391
- Hillebrandt, W., & Wolff, R.G. 1985, in *Nucleosynthesis-Challenges and New Developments*, ed. W.D. Arnett and J.M. Truran, (Chicago: Univ. of Chicago), 131
- Hillebrandt, W., Nomoto, K., & Wolff, R.G. 1984, *A&A*, 133, 175
- Hirata, D., Sumiyoshi, K., Tanihata, I., Sugahara, Y., Tachibana, T., & Toki, H. 1997, *Nucl. Phys. A*, 616, 438c
- Hix, W. R., Messer, O. E. B., Mezzacappa, A., Liebendoerfer, M., Sampaio, J., Langanke, K., Dean, D. J., & Martínez-Pinedo, G. 2003, *Phys. Rev. Lett.*, 91, 201102
- Horiguchi, T., Tachibana, T., Koura, H., & Katakura, J. 2000, *Chart of the Nuclides*, JAERI
- Ishizuka, C. 2005, Ph.D. thesis, Hokkaido University, Sapporo, Japan
- Janka, H.-Th., Buras, R., Kitaura Joyanes, F. S., Marek, A., & Rampp, M. 2004, in *Proc. 12th Workshop on Nuclear Astrophysics*, in press (astro-ph/0405289)
- Kotake, K., Yamada, S. & Sato, K. 2003, *ApJ*, 595, 304
- Kotake, K., Sawai, H., Yamada, S. & Sato, K. 2004, *ApJ*, 608, 391
- Lattimer, J. M., & Swesty, F. D. 1991, *Nucl. Phys. A*, 535, 331
- Langanke, K., & Martinez-Pinedo, G. 2003, *Rev. Mod. Phys.*, 75, 819
- Liebendörfer, M., Mezzacappa, A., Thielemann, F.-K., Messer, O. E. B., Hix, W. R., & Bruenn, S. W. 2001, *Phys. Rev. D*, 63, 103004
- Liebendörfer, M., Messer, O. E. B., Mezzacappa, A., Hix, W. R., Thielemann, F.-K., & Langanke, K. 2002, in *Proc. 11th Workshop on Nuclear Astrophysics*, ed. W. Hillebrandt & E. Müller (Garching: Springer), 126
- Liebendörfer, M., Messer, O. E. B., Mezzacappa, A., Bruenn, S. W., Cardall, C. Y., & Thielemann, F.-K. 2004, *ApJS*, 150, 263

- Liebendörfer, M., Rampp, M., Janka, H.-Th., & Mezzacappa, A. 2005, *ApJ*, 620, 840
- Maxwell, O. V. 1987, *ApJ*, 316, 691
- Mezzacappa, A., & Bruenn, S. W. 1993, *ApJ*, 405, 669
- Mezzacappa, A., & Bruenn, S. W. 1993, *ApJ*, 410, 740
- Mezzacappa, A., Liebendörfer, M., Messer, O. E. B., Hix, W. R., Thielemann, F.-K., & Bruenn, S. W. 2001, *Phys. Rev. Lett.*, 86, 1935
- Misner, C. W., & Sharp, D. H. 1964, *Phys. Rev. B*, 136, 571
- Möller, P., Nix, J. R., Myers, W. D., & Swiatecki, W. J. 1995, *Atomic Data Nucl. Data Tables*, 59, 185
- Ozawa A. *et al.*, 2001, *Nucl. Phys. A*, 691, 599
- Rampp M. 2000, Ph.D. Thesis, Max-Planck Institute for Astrophysics, Garching, Germany
- Rampp, M., & Janka, H.-Th. 2000, *ApJ*, 539, L33
- Rampp, M., & Janka, H.-Th. 2002, *A&A*, 396, 361
- Rosswog, S. & Davies, M. B. 2003, *MNRAS*, 345, 1077
- Serot, B.D., & Walecka, J.D. 1986, in *Advances in Nuclear Physics Vol. 16*, ed. J.W. Negele and E. Vogt (New York: Plenum Press), 1
- Shen, H., Toki, H., Oyamatsu, K., & Sumiyoshi, K. 1998, *Nucl. Phys. A*, 637, 435
- Shen, H., Toki, H., Oyamatsu, K., & Sumiyoshi, K. 1998, *Prog. Theor. Phys.*, 100, 1013
- Sugahara, Y., & Toki, H. 1994, *Nucl. Phys. A*, 579, 557
- Sugahara, Y., Sumiyoshi, K., Toki, H., Ozawa, A., & Tanihata, I. 1996, *Prog. Theor. Phys.*, 96, 1165
- Sumiyoshi, K., Kuwabara, H., & Toki, H. 1995, *Nucl. Phys. A*, 581, 725
- Sumiyoshi, K., Oyamatsu, K., & Toki, H. 1995, *Nucl. Phys. A*, 595, 327
- Sumiyoshi, K., Suzuki, H., & Toki, H. 1995, *A&A*, 303, 475
- Sumiyoshi, K., & Ebisuzaki, T. 1998, *Parallel Computing*, 24, 287

- Sumiyoshi, K., Suzuki, H., Otsuki, K., Terasawa, M., & Yamada, S. 2000, PASJ, 52, 601
- Sumiyoshi, K., Terasawa, M., Mathews, G. J., Kajino, T., Yamada, S., & Suzuki, H. 2001, ApJ, 562, 880
- Sumiyoshi, K., Suzuki, H., Yamada, S., & Toki, H. 2004, Nucl. Phys. A, 730, 227
- Suzuki H. 1990, Ph.D. thesis, University of Tokyo, Tokyo, Japan
- Suzuki H. 1993, in Proceedings of the International Symposium on Neutrino Astrophysics: Frontiers of Neutrino Astrophysics, ed. Y. Suzuki and K. Nakamura (Tokyo:Universal Academy Press Inc.), 219
- Suzuki H. 1994, in Physics and Astrophysics of Neutrinos, ed. M. Fukugita and A. Suzuki (Tokyo:Springer-Verlag), 763
- Suzuki T. *et al.*, 1995, Phys. Rev. Lett., 75, 3241
- Swesty, F. D., Lattimer, J. M., & Myra, E. S. 1994, ApJ, 425, 195
- Thompson, T. A., Burrows, A., & Pinto, P. 2003, ApJ, 539, 865
- Timmes, F. X., & Arnett, D. 1999, ApJS, 125, 277
- Vretenar, D., Niksic, T., & Ring, P. 2003, Phys. Rev. C, 68, 024310
- Walder, R., Burrows, A., Ott, C. D., Livne, E., & Jarrar, M. 2004, submitted to ApJ (astro-ph/0412187)
- Woosley, S. E., & Weaver, T. 1995, ApJS, 101, 181
- Yamada, S. 1997, ApJ, 475, 720
- Yamada, S., Janka, H.-Th., & Suzuki, H. 1999, A&A, 344, 533

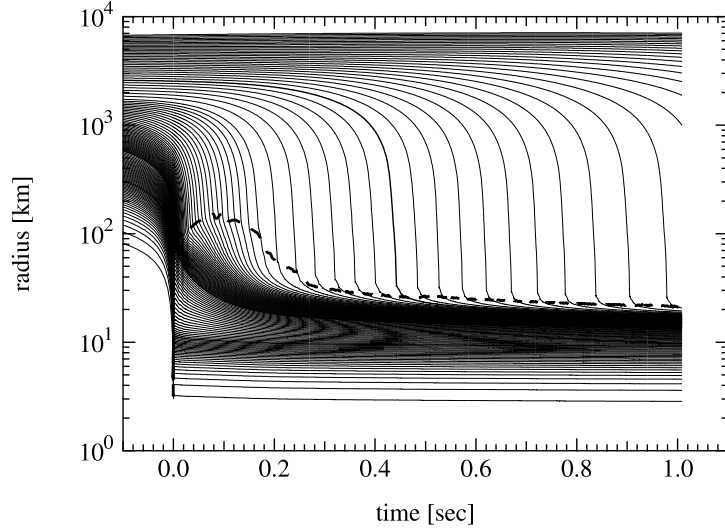


Fig. 1.— Radial trajectories of mass elements of the core of $15M_{\odot}$ star as a function of time after bounce in model SH. The location of shock wave is displayed by a thick dashed line.

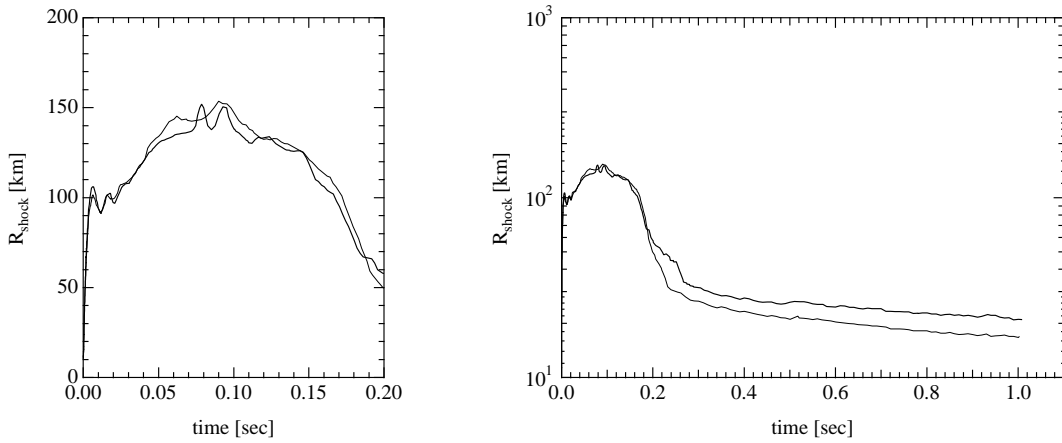


Fig. 2.— Radial positions of shock waves in models SH and LS are shown by thick and thin lines, respectively, as a function of time after bounce. The evolutions at early and late times are displayed in left and right panels, respectively. Small fluctuations in the curves are due to numerical artifact in the procedure to determine the shock position from a limited number of grid points.

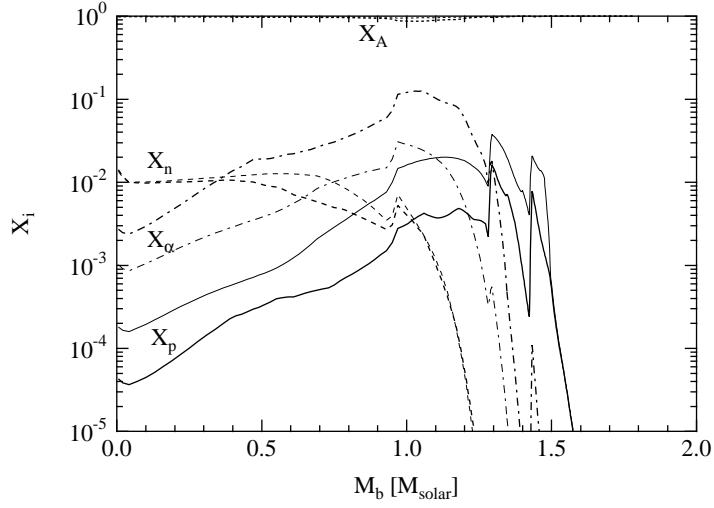


Fig. 3.— Mass fractions in the supernova cores are shown as a function of baryon mass coordinate at the time when the central density reaches 10^{11} g/cm³. Solid, dashed, dotted and dot-dashed lines show mass fractions of protons, neutrons, nuclei and alpha particles, respectively. The results for models SH and LS are shown by thick and thin lines, respectively.

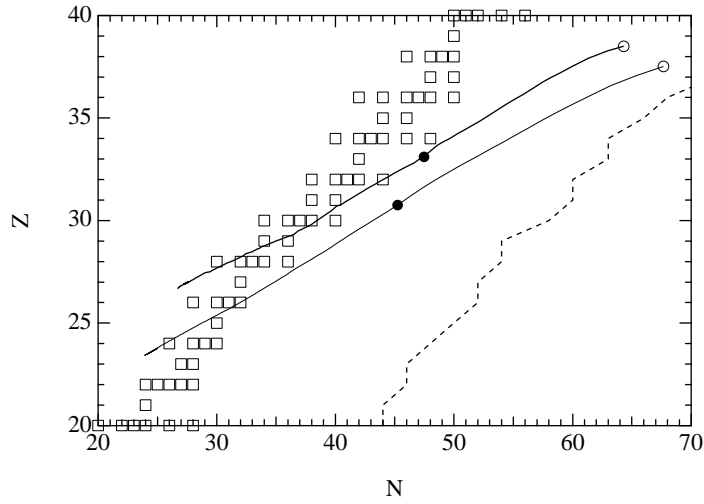


Fig. 4.— Nuclear species appear in supernova cores are shown in the nuclear chart. Stable nuclei and the neutron drip line (Horiguchi et al. 2000) are shown by open square symbols and dashed line, respectively. Nuclear species at the center of the core are marked by solid circle ($\rho_c=10^{11}$ g/cm³) and open circle ($\rho_c=10^{12}$ g/cm³) symbols. The results for models SH and LS are shown by thick and thin lines, respectively.

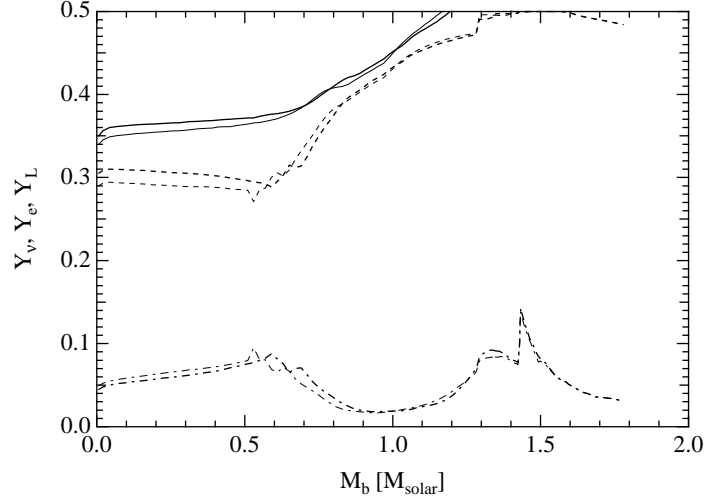


Fig. 5.— Lepton, electron and neutrino fractions at bounce are shown as a function of baryon mass coordinate by solid, dashed and dot-dashed lines, respectively. The results for models SH and LS are shown by thick and thin lines, respectively.

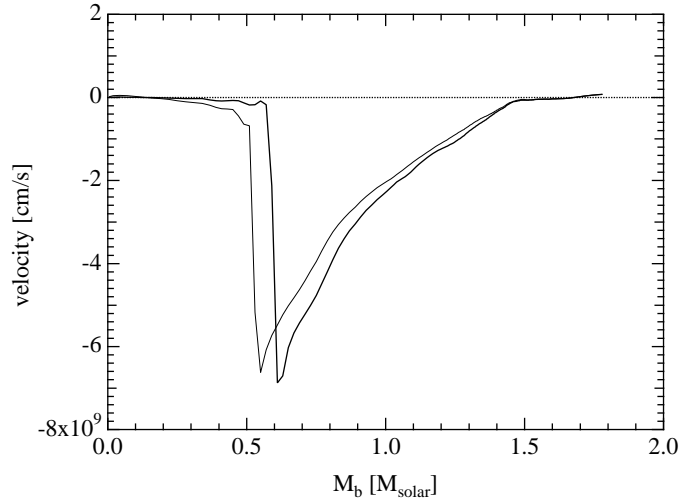


Fig. 6.— Velocity profiles at bounce are shown as a function of baryon mass coordinate. The results for models SH and LS are shown by thick and thin lines, respectively.

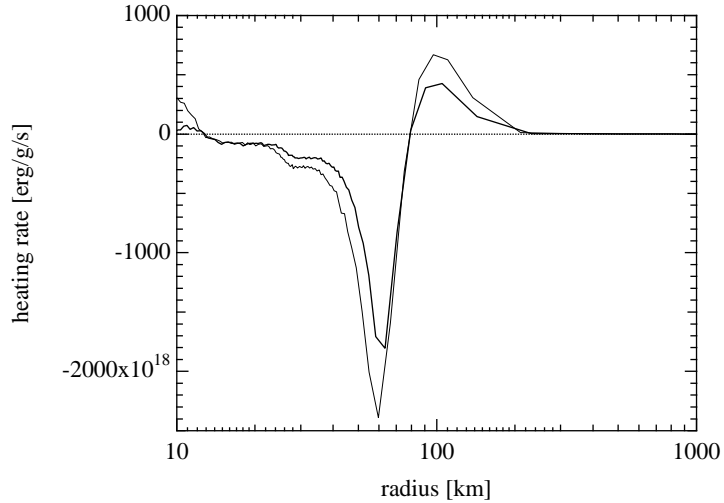


Fig. 7.— Heating rates at $t_{pb}=150$ ms in two models are shown as a function of radius. Notation is the same as in Fig. 6.

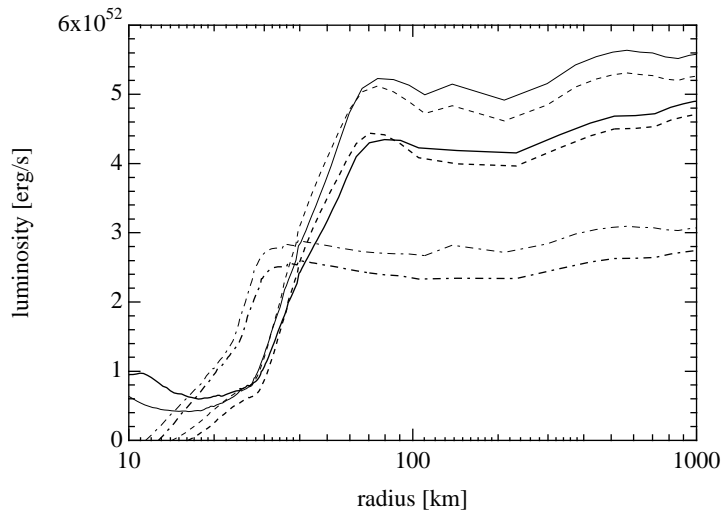


Fig. 8.— Luminosities of ν_e , $\bar{\nu}_e$ and $\nu_{\mu/\tau}$ around the heating region are shown by solid, dashed and dot-dashed lines, respectively, as a function of radius at $t_{pb}=150$ ms. The results for models SH and LS are shown by thick and thin lines, respectively.

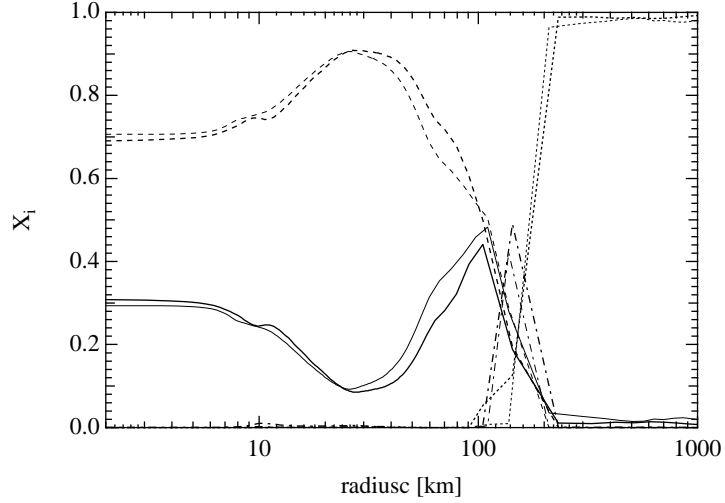


Fig. 9.— Mass fractions in dense matter around the heating region are shown as a function of radius at $t_{pb}=150$ ms. Notation is the same as in Fig. 3.

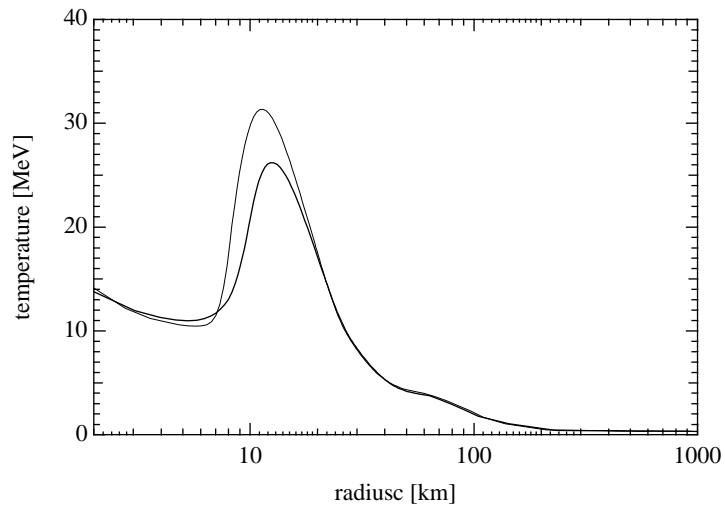


Fig. 10.— Temperature profiles at $t_{pb}=150$ ms for two models are shown as a function of radius. Notation is the same as in Fig. 6.

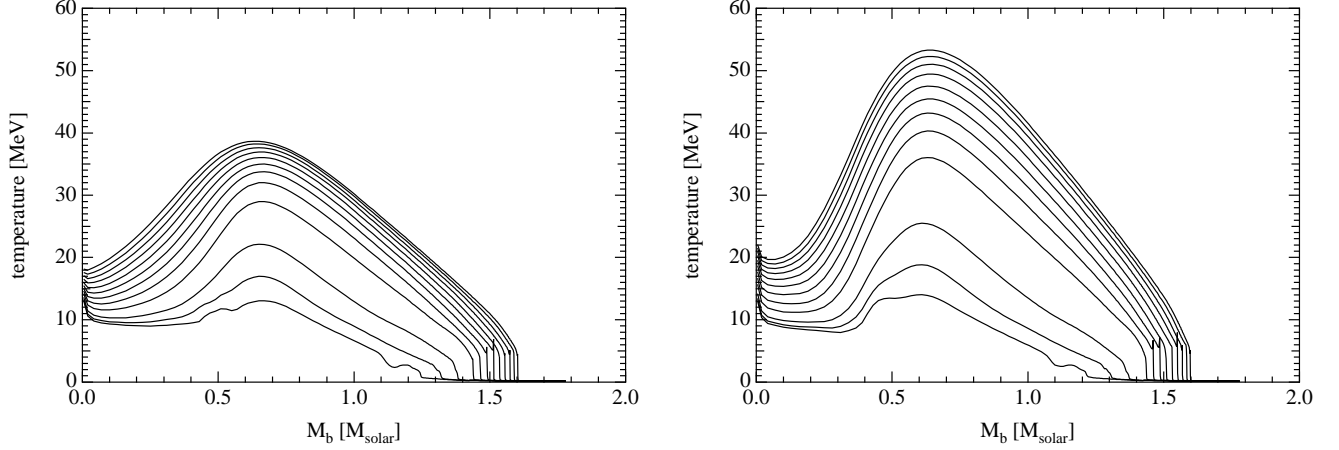


Fig. 11.— Snapshots of temperature profiles as a function of baryon mass coordinate from $t_{pb}=20$ ms to $t_{pb}=1000$ ms in models SH (left) and LS (right). Note that small peaks around the central grid are artificial due to the numerical treatment.

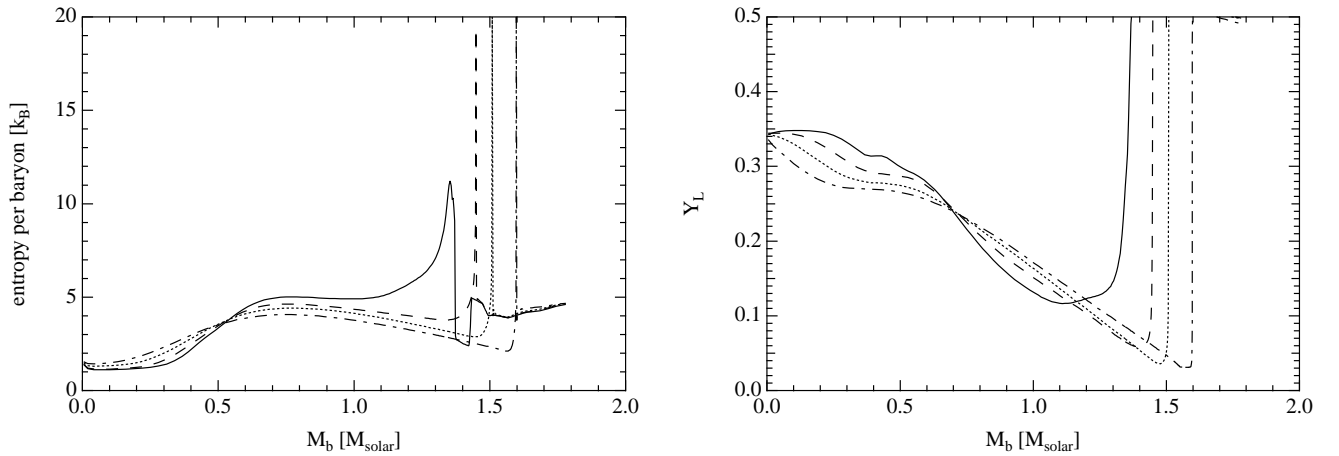


Fig. 12.— Snapshots of entropy (left) and lepton fraction (right) profiles in model LS are shown as a function of baryon mass coordinate at $t_{pb}=100$ ms (solid), $t_{pb}=250$ ms (dashed), $t_{pb}=500$ ms (dotted) and $t_{pb}=1000$ ms (dot-dashed).

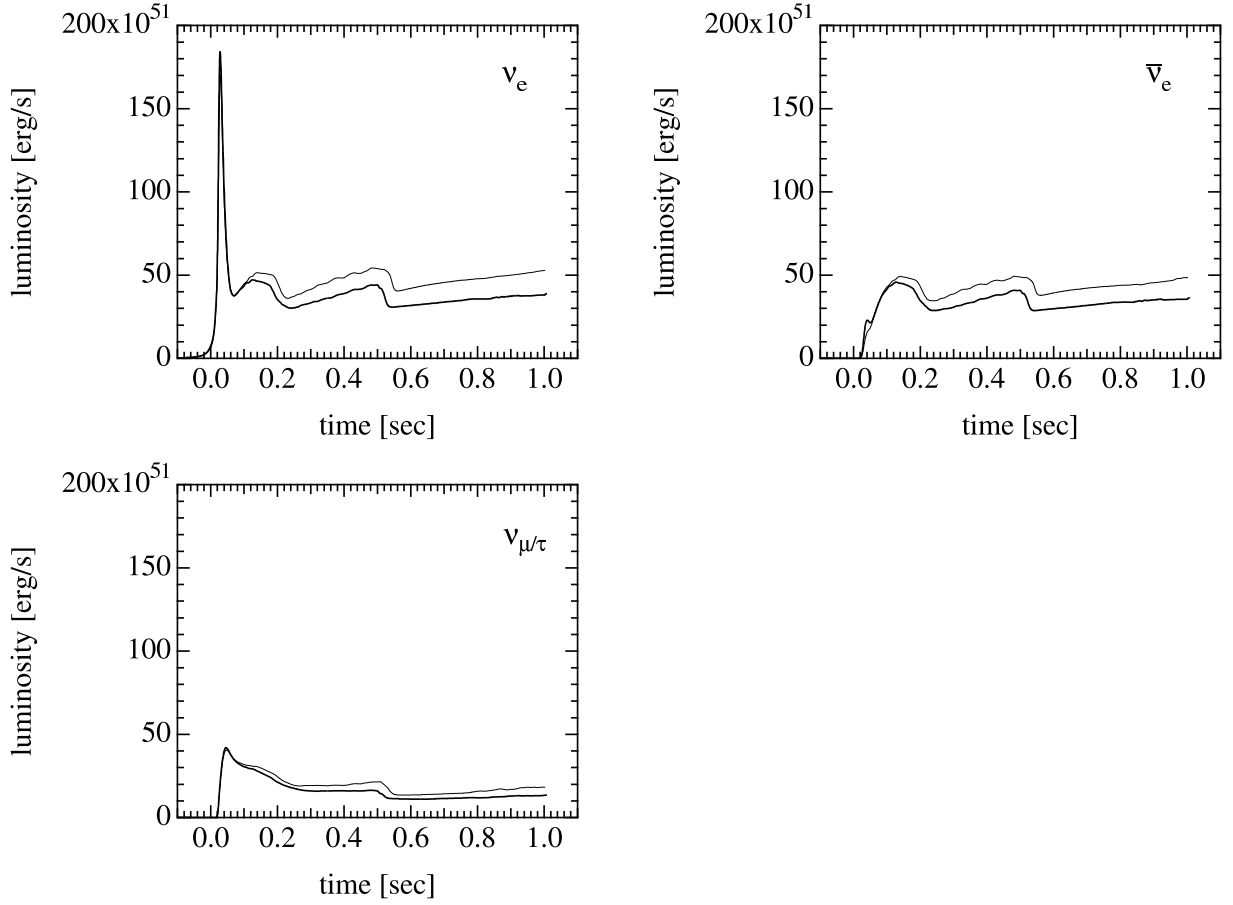


Fig. 13.— Luminosities of ν_e , $\bar{\nu}_e$ and $\nu_{\mu/\tau}$ are shown as a function of time after bounce. Notation is the same as in Fig. 6. Kinks around $t_{pb}=500$ ms are due to numerical artifact due to the rezoning of mass coordinate. See the main text for details.

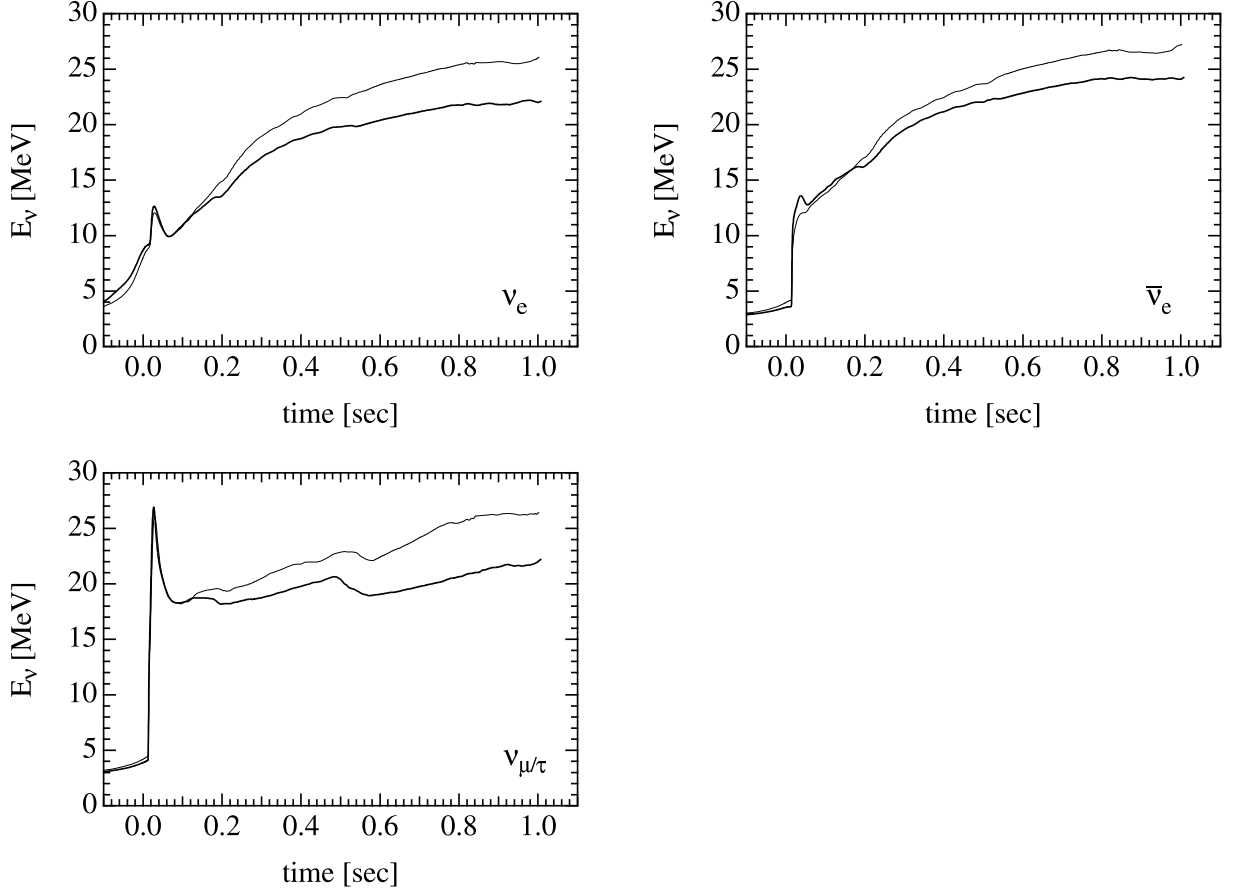


Fig. 14.— Average energies of ν_e , $\bar{\nu}_e$ and $\nu_{\mu/\tau}$ are shown as a function of time after bounce. Notation is the same as in Fig. 13. Kinks around $t_{pb}=500$ ms are due to numerical artifact due to the rezoning of mass coordinate. See the main text for details.